Double- and multi-slit interference in photodetachment from nanometer organic molecular anions

Cite as: J. Chem. Phys. **150**, 244302 (2019); https://doi.org/10.1063/1.5100799
Submitted: 20 April 2019 . Accepted: 07 June 2019 . Published Online: 26 June 2019

Yuan Liu, Chuan-Gang Ning, and Lai-Sheng Wang

The Journal of Chemical Physics ARTICLE scitation.org/journal/jcp

Double- and multi-slit interference in photodetachment from nanometer organic molecular anions

Cite as: J. Chem. Phys. 150, 244302 (2019); doi: 10.1063/1.5100799
Submitted: 20 April 2019 • Accepted: 7 June 2019 •
Published Online: 26 June 2019 • Corrected: 29 July 2019

Yuan Liu,[1] Chuan-Gang Ning,[2,3,a)] and Lai-Sheng Wang[1,a)]

AFFILIATIONS

[1] Department of Chemistry, Brown University, Providence, Rhode Island 02912, USA
[2] State Key Laboratory of Low-Dimensional Quantum Physics, Department of Physics, Tsinghua University, Beijing 10084, China
[3] Collaborative Innovation Center of Quantum Matter, Beijing, China

[a)] **Authors to whom correspondence should be addressed:** ningcg@tsinghua.edu.cn and Lai-Sheng_Wang@brown.edu

ABSTRACT

We present the predictions of double-slit and multislit interference of photoelectrons from a nanometer-size molecular negative ion. The interference clearly appears in both photoelectron angular distributions and photodetachment cross sections. In contrast to the diatomic photoelectron interference via the X-ray photon, the interference in the nanometer-size negative ions can be readily observed via a visible or extreme ultraviolet laser. Therefore, the phenomenon can be realized on a table-top setup, instead of a large accelerator.

I. INTRODUCTION

Wave-particle duality is the signature of quantum mechanics, and the interference of particles originated from this duality has been extensively studied as either a test of fundamental physics or a sensitive probe for structures of matter in systems ranging from electrons to large organic molecules.[1–6] Photoelectron spectroscopy, aiming to explore the structure of matters in the most microscopic level, provides an ideal tool to investigate such interference effects. In photoionization or photodetachment experiments, photoelectrons can escape from the molecules as matter waves if the photon energy is higher than the binding energy of electrons in molecules. The detailed information about the electronic,[7] vibrational,[8] rotational,[9] and geometric[10] structures of molecules is encoded in the kinetic energy and interference of photoelectrons.[11] The outgoing photoelectrons are usually represented by partial waves. Photoelectron interference happens due to the relative phase shift between different partial waves. While partial wave interference is ubiquitous in all photodetachment and photoionization processes,[12,13] there is, however, another not so common yet intriguing interference originating from the spatial coherence of molecular orbitals (MOs), often called double-slit or dual-center photoelectron interference[10,14–17] due to its similarities with classical Young's double slit interference in optics. In the present work, we will discuss this type of interference.

Photoelectron interference can be characterized by the oscillations in the photoelectron angular distribution (PAD) and in the total cross section, which are the major observables in photoionization or photodetachment experiments in the gas phase. They are defined in laboratory frame (LF) for single photon ionization or detachment of randomly oriented molecules by linearly polarized light in the following way:

$$\frac{d\sigma}{d\Omega} = \frac{\sigma_T}{4\pi}[1 + \beta P_2(\cos\theta)], \tag{1}$$

where $\frac{d\sigma}{d\Omega}$ is the differential cross section of photodetachment with respect to the solid angle Ω, σ_T is the total cross section, β is the so-called anisotropy parameter to describe the angular distribution of photoelectrons, P_2 is the second-order Legendre polynomial, and θ is the angle between the photon polarization and the ejection direction of photoelectrons. Equation (1) also suggests that in

LF, the PAD has a relatively simple structure fully characterized by a second-order Legendre polynomial in this case (note that for the multiphoton process, higher order Legendre polynomials will also play a role), which ranges from fully spherical symmetric to a *p*-orbital-like shape. The oscillation period of the photoelectron cross section and PAD with respect to probing photon energy depends on the distance between the electronic density centers in molecules according to Cohen and Fano.[14] On the other hand, in molecular frame (MF), the PAD will usually be more complicated and have more nodal structures due to no average of random orientations.[18] In this case, interference manifests itself as changes of nodal structures of MF PAD. However, most of the theoretical and experimental studies of photoelectron interference are photoionization of neutral molecules, where the long-range Coulomb interaction would induce additional phase shift of photoelectrons which can complicate the situation by mixing with the initial phase shift due to spatial coherence of the molecular orbital itself. Moreover, the strong Coulomb attraction between electrons and a *positive* molecular core usually requires photons with an energy of tens or hundreds of eV to ionize the electrons to continuum, which poses stringent experimental requirements such as a free electron laser.[7] By contrast, photodetachment of negative ions (anions) from their valence orbitals only requires photons with much less energy (typically several eV). Since there is only weak short-range interaction (this short-range interaction typically decays much faster than the Coulomb interaction) between the detached electron and the remaining *neutral* molecular core, the additional phase shift will also be smaller. As a result, such photodetachment experiments can usually be done with only a table-top setup and a UV-visible laser. Despite great experimental advantages, photoelectron interference via detachment of negative ions surprisingly remains largely unexplored. Mabbs *et al.* applied a LCMO (linear combination of molecular orbitals) based[19] dual center approach to explain the strong similarities of PAD for detachment from monomer- and dimer-anion based CO_2 cluster anions[20] as well as the oscillation of PAD from I_2^- as I-I distance increases in the photodissociation experiment with the largest I-I distance probed as 36 Å,[21,22] while photoelectron interference of large molecular anions has not been experimentally observed nor theoretically studied. From the de Broglie relation[23]

$$\lambda_e = \frac{h}{p_e} \tag{2}$$

(where h is Planck's constant), the larger size of molecules (thus also the electron de Broglie wavelength λ_e) means lower electron momentum p_e is required to observe the interference effect. This also reduces the photon energy required in such an experiment. Moreover, a larger size will give more fruitful interference phenomena and enable us to go beyond double-slit settings to answer the question whether multislit interference is possible and how it is like for photoelectrons.

The challenge for studying photoelectron interference in molecules with a large size lies in the dense electronic, vibrational, and rotational states on the experimental side and the prohibited computational cost on the theoretical side. The detailed interference structures may be washed out in experiments if the energy resolution is not high enough to resolve each electronic state. On the theoretical side, the accuracy of calculations of PAD relies on the quality of the electronic wavefunction of the molecule, especially the parts far from the nuclei. The electronic wavefunctions of molecular anions are usually very diffuse and require high-quality diffuse basis sets,[24,25] which greatly increases the computational cost. PAD calculations based on the Dyson orbital obtained from many-body theory such as coupled cluster are only practical for small systems[25] due to the large computational cost.

Recently, we introduced a new method based on the density functional theory (DFT).[26] Our method can handle the large molecular anions with a relatively low cost. With this method, we present the predictions of the PAD and cross section of a nanometer size long chain organic molecular anion, deprotonated 3, 3′-dihydroxy-16, 17, 18, 16′, 17′, 18′-hexanor-Φ, Φ-carotene anion ($C_{34}H_{34}O_2^-$, DDHHC$^-$). Four outermost molecular orbitals (MOs) are investigated in both MF and LF where linearly polarized light is used. The highest occupied molecular orbital (HOMO) and the next HOMO (HOMO-1) are the delocalized π-type orbitals corresponding to the conjugation in the carbon chain. The HOMO-3 and HOMO-4 are mainly from the lone paired electrons of the two oxygen atoms at the ends of the molecular chain. Besides the traditional double-slit interference effect in HOMO-3 and HOMO-4, multislit interference also emerges for HOMO and HOMO-1 as the photon energy increases. On the experimental side, the recent development of the velocity mapping imaging method in combination with the cold ion trap has significantly improved the energy resolution of photoelectron spectroscopy. This powerful method has overcome the difficulty of resolving the dense quantum states of large molecular anions.[27–30]

II. METHODOLOGY

To calculate the photoelectron cross sections and PAD of each MO, the geometry of DDHHC$^-$ is optimized using the Becke 3-parameter Lee-Yang-Parr[31–34] (B3LYP) flavor of DFT with the 6-311++G** Gaussian type basis set, yielding a lowest energy geometry with C_{2h} symmetry. Its electronic wavefunction is subsequently calculated with the Slater type TZVP basis set because its asymptotic form $e^{-\xi r}$ correctly describes the electronic wavefunction at the larger distance, which is important in the calculations of photodetachment.[26] Note that the geometry of the molecule is fixed at the optimized one, and all vibration induced nuclei motion is ignored. The ADF[35] and Gaussian packages[36] are used for all the electronic structure calculations. The wavefunction is then used as the initial state to calculate the cross sections and PAD at various photon energy (or photoelectron kinetic energy). The electric dipole approximation is used since the molecular length is much shorter than the photon wavelength in the energy regime we explored (at the largest electron kinetic energy of 20 eV, the molecular length is still only about 6% of the photon wavelength). Final states of electrons in continuum are represented by a plane wave where interactions between the detached electron and the neutral molecular core are ignored. The plane wave is further approximated by a truncated expansion where we include enough high-order angular momentum contributions for the convergence of results. The average over random orientation of gas molecules is implemented analytically in LF calculations. In MF calculations, we simply fix the molecule orientation and laser polarization. We have benchmarked our method against experimental results for various anions, where excellent agreement between the two is achieved for both PAD and photodetachment

TABLE I. Detachment energy of the molecular orbitals studied.

Orbital	Symmetry	Detachment energy (eV)
HOMO	A_u	2.0
HOMO-1	B_g	3.1
HOMO-3	A_g	4.4
HOMO-4	B_u	4.4

cross section. Details of the theoretical approach and benchmark can be found in Ref. 26. The binding energies of MOs are obtained from their Kohn-Sham orbital energies according to Koopmans' theory,[37,38] as shown in Table I. For consistency, in all MF calculations, the molecule is aligned along the *y*-axis and lies within the *xy*-plane. The electric vector of the linearly polarized light is parallel to the *y*-axis. We should note that although Kohn-Sham orbitals are intrinsically based on a single-particle picture, they capture the essential spatial coherence of the orbital wavefunctions where the interference originates from in the present work.

III. RESULTS AND DISCUSSIONS

A. Double-slit interference

The main contribution to HOMO-3 and HOMO-4 of $DDHHC^-$ is the lone pair electrons localized on the two oxygen atoms at the ends of the chain. Belonging to the A_g (B_u) irreducible representation of the C_{2h} point group, HOMO-3 (HOMO-4) is symmetric (antisymmetric) with respect to the inversion operation and C_2 rotation; see the inset of Fig. 1(b) for HOMO-3. The ejected photoelectron from this orbital has two equivalent contributions from both oxygen atoms, and these two equivalent parts produce a double-slit interference [Fig. 1(a)]. Because the symmetry of HOMO-3 and HOMO-4 is opposite, their interference is similar but opposite in phase. As an example, we will discuss HOMO-3 in detail in the rest of Sec. III A.

As the detachment photon energy increases (so does the kinetic energy of the photoelectron), the intensity of the total photoelectron yield (cross section) shows an oscillatory behavior [red lines in Fig. 1(a)]. The PAD also changes periodically as indicated by the oscillation of the anisotropy parameter β [black lines in Fig. 1(a)]. It should be noted that the maximal angular momentum quantum L_m of partial waves must be high enough to describe the photoelectrons due to the multinode and multicenter of molecular orbitals. For the purpose of comparison, Fig. 1 shows the results at $L_m = 4$ (dashed lines) and $L_m = 18$ (solid lines). Here, $L_m = 4$ is a typical value where the maximal partial wave angular momentum is the maximal angular momentum l in the atomic basis set plus one in the dipole approximation.[25,26] It can be seen that $L_m = 4$ is not enough for describing the detached photoelectrons. With the test for even larger L_m, we found that $L_m = 18$ has approached the convergence. In Fig. 1(a), the total cross section and β are always in phase with each other in the interference since their oscillation has the same physical origin. The position of the interference maxima does not change much with increasing L_m, which means that small partial wave angular momentum truncation, although cannot describe the photodetachment very well, is enough to qualitatively capture the essential physics of the interference.

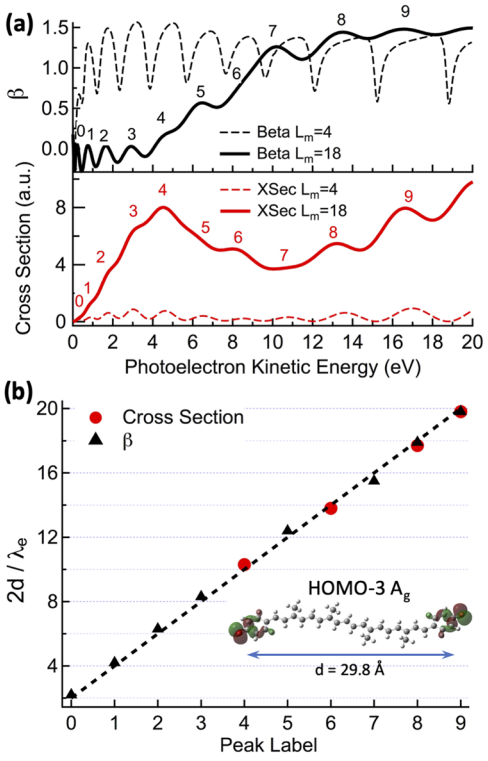

FIG. 1. Photoelectron double-slit interference from HOMO-3 of $DDHHC^-$. (a) Total photoelectron cross section (red lines) and PAD anisotropy parameter β (black lines) as a function of kinetic energies of photoelectrons at the different angular momentum maximum truncation $L_m = 4$ (dashed lines) and $L_m = 18$ (solid lines). Positions of maxima are labeled as 0–9. (b) The relative ratio of the distance d to the de Broglie wavelength of photoelectrons λ_e vs the peak label. The inset of (b) shows the molecular structure of $DDHHC^-$ (carbon in gray, hydrogen in white, and oxygen in red) and HOMO-3 orbital. The color indicates the phase of the wavefunction. The weighted distance between the two electronic clouds localized on the two oxygen atoms is $d = 29.8$ Å.

To understand the double-slit nature of the interference more intuitively, the weighted electronic density distance d between the charge distributions of HOMO-3 is determined to be 29.8 Å (about the length of the molecule), which is the effective separation between the molecular slits. The de Broglie wavelength λ_e of the photoelectrons at peaks labeled as 0 through 9 in Fig. 1(a) is then calculated from the de Broglie relation in Eq. (2). Ratios of $2d/\lambda_e$ are plotted for each peak in both total cross section and β [Fig. 1(b)]. It is known from classical Young's double-slit interference: when the path difference from the two slits to any given point in space is an integer of the wavelength, constructive interference will appear, while destructive interference shows up when the path difference is a half-integer of the wavelength. Strikingly simple relations also appear in the photoelectron interference here as in Fig. 1(b), namely, $2d/\lambda_e$ is always an even number for all the maxima in the interference, which implies its double-slit nature.

The double-slit interference is even more evident in MF since there is no orientation averaging effect. For illustrative purpose, we set the laser polarization along the molecular carbon backbone (the y-axis) for two reasons: to mimic the classical double-slit experiment where the light propagation direction is perpendicular to the double-slit (thus, the polarization will be parallel to the slits or here the molecular chain) and the cross section is two orders of magnitude greater in parallel polarization than that in perpendicular polarization. Figure 2 displays the 3D MF PAD at peak 2 [panel (a)] and 3 [panel (b)] [as labeled in Fig. 1(a)] with a 2D cut through the xy-plane ($z = 0$) as well as the orientation of HOMO-3, and the laser polarization is indicated by the red double arrows. A larger value in the plot along a certain direction means a greater probability that photoelectrons are ejected toward this direction (see the caption of Fig. 2 for more details). In the C_{2h} point group, since HOMO-3 belongs to A_g irrep and the laser polarization is along the y-axis with a symmetry of B_u, the detached photoelectron should have partial waves also with B_u symmetry. However, MF PAD is essentially the absolute square of these partial waves where all the total phase information will be lost and reduced to simply symmetric with respect to all symmetry operations in the group, which agrees with the results in Fig. 2. Moreover, there are several lobes appearing at different directions, and the number of lobes increases from six (peak 2) to eight (peak 3) in half of the xy-plane, which is equal to the ratio of $2d$ over λ_e as shown in Fig. 1(b). Similar characteristics also appear for other peaks in the high kinetic energy region. The orientations of the maxima in Fig. 2 generally are not symmetric with respect to the slit normal direction (the x-axis) because the molecule is not perfectly linear in the xy-plane.

It should be noted that the experimental observation of the double-slit interference from HOMO-3 might be difficult because its antibonding counterpart HOMO-4 lies very close in energy. The energy difference is less than 0.1 eV according to DFT calculations. The out-of-phase interference signals from them may cancel with each other to some degree, leaving the net oscillation in the total cross section and anisotropy parameter β even smaller or negligible.

B. Multislit interference

As shown in Fig. 3(b), HOMO of $DDHHC^-$ has 15 similar repeating units with a unit-distance d_m of about 2.4 Å, and HOMO-1 has 14. The repeating structures can form multislit interference in the photodetachment experiment. HOMO and HOMO-1 are two well-separated MOs with an orbital energy difference of about 0.9 eV, which are also isolated from other lower lying molecular orbitals according to our DFT calculations. This makes them to be easily resolved in the photodetachment experiment. The HOMO orbital has A_u symmetry and is symmetric about $C_2(z)$ rotation and antisymmetric with respect to the inversion i and mirror operation σ_h. HOMO-1 has B_g symmetry, which is antisymmetric with $C_2(z)$ rotation and mirror operation σ_h and symmetric about inversion operation i. The two MOs intuitively can be viewed as molecular multislits, with a slit distance d_m equal to the distance between every two nodes as labeled in Fig. 3(b) with opposite phases.

Figure 3 shows the predicated β parameter and cross sections vs the kinetic energy of photoelectrons. At the lower kinetic energy region (0–4 eV), the total cross section is greatly suppressed [the negligible total cross section at the low kinetic energy range in Fig. 3(a)] because the length scale of the electronic wavefunction (the slit distance d_m) in HOMO and HOMO-1 is much shorter than the de Broglie wavelength of the low kinetic energy electrons. From the partial wave viewpoint, the suppression is due to the high

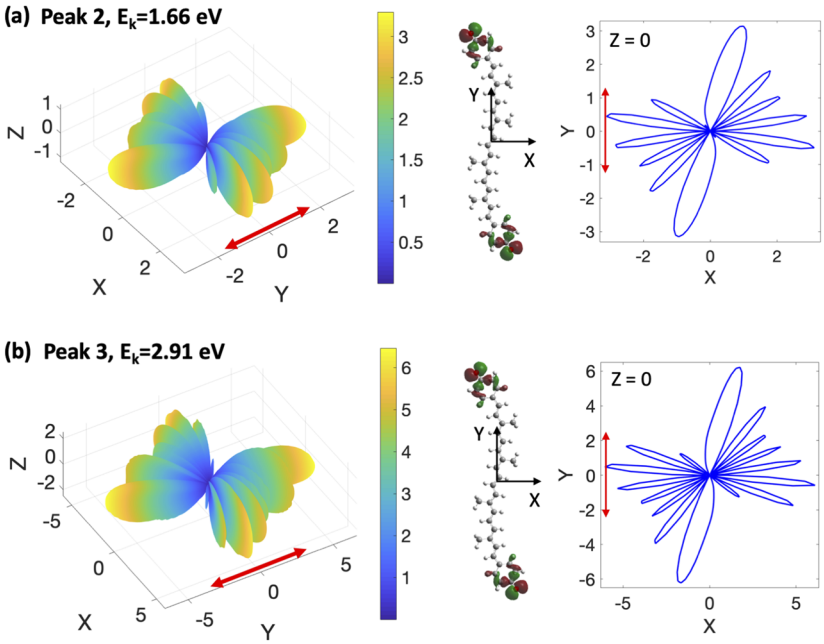

FIG. 2. 3D MF PAD of HOMO-3 (A_g) of $DDHHC^-$ for different photoelectron kinetic energies, corresponding to peak 2 [panel (a)] and 3 [panel (b)] in Fig. 1(b), with a 2D cut of the PAD through the $z = 0$ plane (the xy plane) in solid blue lines on the right of each panel, and the relative orientation of the molecular chain with HOMO-3 is also shown in the middle of each panel. The red double arrows in each panel indicate the laser polarization. The probability of emitting photoelectrons in a direction (θ, ϕ) is represented by the color bar.

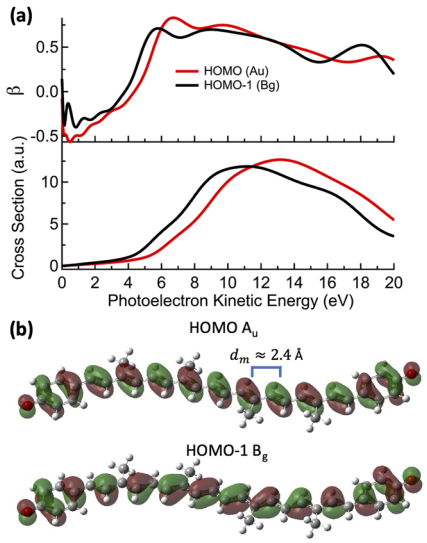

FIG. 3. Photoelectron multislit interference from HOMO and HOMO-1 of $DDHHC^-$. (a) Total photoelectron cross section and anisotropy parameter β of HOMO (A_u, red curves) and HOMO-1 (B_g, black curves) as a function of photoelectron kinetic energy at an angular momentum truncation of L_m = 18 to guarantee convergence. (b) HOMO and HOMO-1 (see the caption of Fig. 1 for details). The molecular multislit width $d_m \approx 2.4$ Å is also labeled as the distance between adjacent electron density distributions with opposite phases.

centrifugal potential, which is proportional to $l(l+1)/r^2$ for the lth partial wave. The existence of multiple nodes in HOMO and HOMO-1 implies that the main contribution of photodetachment is from partial waves with large angular momentum l. Nevertheless, the anisotropy parameter β still shows an oscillatory behavior at the low kinetic energy range, as shown in Fig. 3(a). Such oscillations are due to the interference between partial waves with different angular momentum l. The opposite oscillations of HOMO and HOMO-1 are due to their different orbital symmetry.

As the kinetic energy of photoelectrons increases, a giant resonance appeared in both total cross section and β at $E_k \sim 6$ eV for both HOMO and HOMO-1, corresponding to a de Broglie wavelength of about 5.0 Å, which is roughly twice of the distance d_m. The match of length scale means that the resonance comes from a multislit constructive interference, which only appears when the electron de Broglie wavelength is small enough to probe the fine nodal structure of the molecular orbitals' density distribution; otherwise, an opposite phase electronic wavefunction between adjacent nodes will be smeared out. This enhancement may also be understood in the following way. When the electron de Broglie wavelength is $\lambda_e = 2d_m$, adjacent slits will simply lie in the two parts of the detached electron's final de Broglie wave with opposite phases, which matches the nodal structure of its initial wavefunction (HOMO and HOMO-1) exactly. This overlap between the initial and final states (the dipole operator only has one node at the origin and thus will not significantly alter the overlap) makes the cross section at this particular energy increase dramatically. In MF, Fig. 4 shows the 3D MF PAD of these two orbitals with a 2D view from the x-axis and orientation of MOs around this resonance energy, featuring four sharp lobes. The initial symmetry of these two orbitals dictates that the final photoelectron scattering wave should have B_g symmetry for HOMO and A_u symmetry for HOMO-1. As a result, the MF PAD (absolute square of the scattering wave) should be symmetric with respect to all the operations in the C_{2h} group which is apparently the case as in Fig. 4. Note that although the MF PAD of these two orbitals is very similar given their similar density distributions, one difference is that the MF PAD has a finite value for $y = 0$ in the case of HOMO-1 [Fig. 4(b)] while zero for HOMO [Fig. 4(a)] due to their different

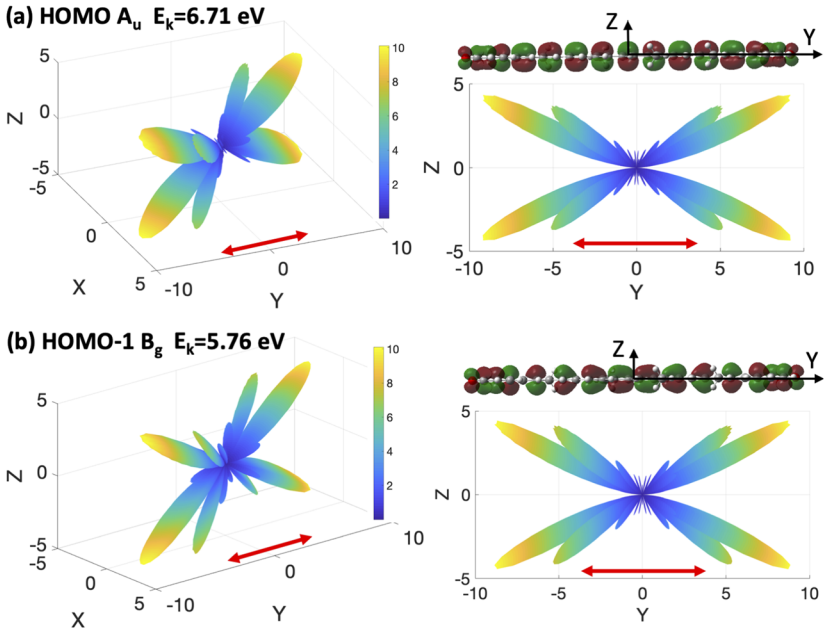

FIG. 4. 3D MF PAD of HOMO [panel (a)] and HOMO-1 [panel (b)] of $DDHHC^-$ for $\lambda_e = 2d_m$, with the view of PAD and MO from the x-axis on the right of each panel, centered at the origin. The red double arrows indicate the direction of the laser polarization. The photoelectron kinetic energy is 6.71 eV for HOMO and 5.76 eV for HOMO-1.

orbital symmetries. In this case, it is not a classical diffraction analogy in optics since grating diffraction usually happens for the light wavelength equal or smaller than the slit distance, while here we have $\lambda_e = 2d_m$.

To directly see the multislit interference of photoelectrons and compare it with classical optics, we must explore a higher photoelectron kinetic energy regime where λ_e is equal or smaller than d_m. Figure 5 shows the 3D MF PAD for $\lambda_e = d_m$ overlapped by the multislit interference calculated from classical wave mechanics as a comparison. To best simulate HOMO (or HOMO-1) electronic density distribution with a classical multislit optical interference setting, we assume a one-dimensional grating along the y-axis with N slits and a grating constant of d_m. We further assume that all slits are identical except that adjacent slits have a light source in opposite phases with a wavelength of λ_e. The slit number N is chosen to match the number of nodes of HOMO ($N = 15$) and HOMO-1 ($N = 14$) in Fig. 3(b). For such a grating, from classical wave mechanics, the final diffraction intensity distribution due to multislit interference is given by

$$I(\theta) \propto \frac{\cos^2\frac{\alpha N}{2}}{\cos^2\frac{\alpha}{2}}, N \text{ is odd}, \tag{3}$$

$$I(\theta) \propto \frac{\sin^2\frac{\alpha N}{2}}{\cos^2\frac{\alpha}{2}}, N \text{ is even}, \tag{4}$$

where $\alpha = 2\pi d_m \sin\theta/\lambda_e$ and θ is measured from the grating normal. These results from Eqs. (3) and (4) are displayed in Fig. 5 with dark red lines. To show its submaxima and fine features, the principal maxima are truncated at a certain radius and overlaid to the 2D MF PAD as viewed from the x-axis on the right of each panel. The full profile is plotted in the black box at the upper part of each panel where the principal lobe forms an angle of 30° with respect to the grating normal as expected. We observe a clear similarity between the diffraction pattern from classical multislit interference and our MF PAD from quantum mechanical calculations. The directions of the principal maxima agree well between each other. The submaxima profiles are also similar in general. The intensity disagreement between MF PAD and classical wave mechanics at the small z region on the left and right sides of the origin is probably due to the deviation of HOMO and HOMO-1 from ideal gratings where each slit is exactly identical. Note that in the case of HOMO, classical wave mechanics predicts a finite intensity along the line of $z = 0$ (the y direction), while the MF PAD result gives zero intensity. This is due to the singularity of the dipole operator (along y) at $z = 0$. Calculations at even shorter de Broglie wavelength $\lambda_e = d_m/4$ ($E_k = 429$ eV) also suggest a multislit interference picture with more maxima at different angles as predicted by the grating equations Eqs. (3) and (4).

In the photodetachment experiments for gas-phase anions, such interference patterns may be difficult to observe due to their random orientation and the atomic nuclei vibrational motion, which will wash out details of interference patterns. To overcome the orientation averaging problem, one method is to partially align the long molecular chain using a femtosecond laser pulse[39–41] or perform a kinematically complete measurement[17] of all molecular fragments after detachment, which would be difficult for large organic molecules. Another possible solution is to synthesize a molecular chain with a macroscopic length, such as the carbon nanotube, so that it can be fixed on an electrode. Previous work suggests that molecular vibrations can significantly change the photodetachment cross sections and anisotropy parameter.[42,43] The following analysis shows that at least the zero-point vibrations will not perturb the interference pattern discussed in the current work. Among a total of 204 normal modes in this molecule, the floppiest one, an out-of-plane bending mode, has a vibrational frequency of about 8 cm^{-1} with a force constant of 0.0003 mDyne/Å. We can then estimate that the relative displacement of atoms in this mode at a zero-point vibrational state would be about 0.07 Å which is about 0.2% of the double slit width and is too small to induce significant changes to the double-slit interference pattern (a shift from maxima to minima for the tenth order interference would require 5% change in the slit width). For multislit interference, this displacement would be about 3% of the slit width, still very small for low order multislit interference. However, the above analysis does suggest the importance

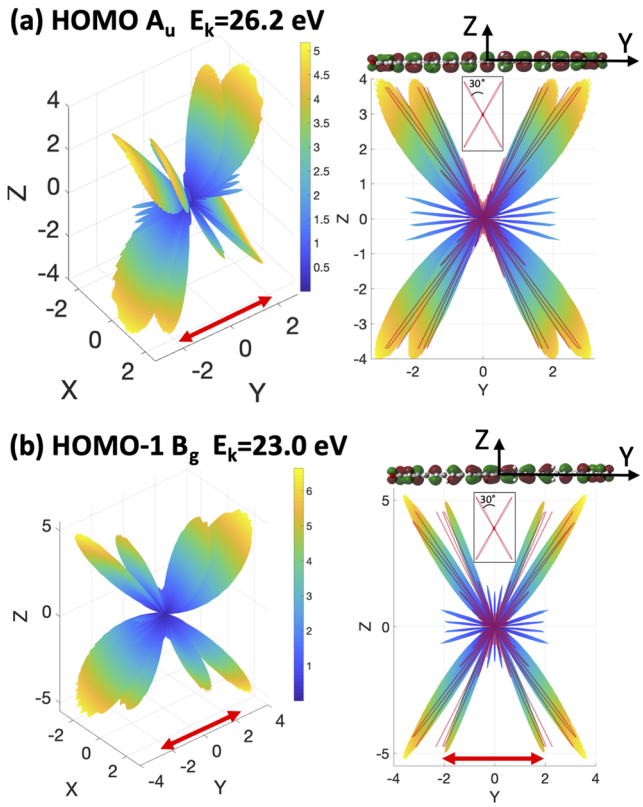

FIG. 5. 3D MF PAD of HOMO [panel (a)] and HOMO-1 [panel (b)] of $DDHHC^-$ for $\lambda_e = d_m$, with the corresponding MO and classical multislit interference diffraction intensity overlaid in the inset (dark red lines) as viewed from the x-axis on the right of each panel. The red double arrows indicate the direction of the laser polarization. The principal maxima of the classical multislit interference results are truncated at a small radius to show the submaxima and fine features, while the full intensity distribution is displayed in the black box as a subplot in the 2D view, where the angle between the principal lobe and the grating normal is labeled as 30°. The photoelectron kinetic energy is 26.2 eV for HOMO and 23.0 eV for HOMO-1.

of low temperature for such experiments in order to minimize the effects of nuclei motion.

IV. CONCLUSION

The present work extends the study of photoelectron interference to the detachment process of large negative ions. We predict the double-slit and multislit interference of photoelectrons from the photodetachment of a nanometer-size molecular negative ion. The interference emerges from the oscillation signatures in both the photoelectron angular distributions and photodetachment cross sections. Thanks to the large size of the negative ion, the interference can be readily observed via a visible or extreme ultraviolet (XUV) laser[44] as opposed to X-ray photon in the previously reported diatomic interference. Therefore, it significantly lowers the experimental barrier for studying such phenomena.

ACKNOWLEDGMENTS

Y.L. gratefully acknowledges the discussions with Professor Brenda Rubenstein as well as the support by the Presidential Fellowship of Brown University. Part of the calculations were conducted using computational resources and service at the Center for Computation and Visualization, Brown University. C.-G.N. thanks the support by the National Natural Science Foundation of China (NSFC) (Grant No. 91736102) and the National key R&D program of China (Grant No. 2018YFA0306504).

REFERENCES

[1] C. Davisson and L. H. Germer, Nature **119**, 558 (1927).
[2] I. Estermann and O. Stern, Z. Phys. A **61**, 95 (1930).
[3] W. Schollkopf and J. P. Toennies, Science **266**, 1345 (1994).
[4] M. Arndt, O. Nairz, J. Vos-Andreae, C. Keller, G. van der Zouw, and A. Zeilinger, Nature **401**, 680 (1999).
[5] S. Gerlich, S. Eibenberger, M. Tomandl, S. Nimmrichter, K. Hornberger, P. J. Fagan, J. Tuxen, M. Mayor, and M. Arndt, Nat. Commun. **2**, 263 (2011).
[6] T. Juffmann, A. Milic, M. Mullneritsch, P. Asenbaum, A. Tsukernik, J. Tuxen, M. Mayor, O. Cheshnovsky, and M. Arndt, Nat. Nanotechnol. **7**, 297 (2012).
[7] M. Ilchen, L. Glaser, F. Scholz, P. Walter, S. Deinert, A. Rothkirch, J. Seltmann, J. Viefhaus, P. Decleva, and B. Langer, Phys. Rev. Lett. **112**, 023001 (2014).
[8] S. E. Canton, E. Plésiat, J. D. Bozek, B. S. Rude, P. Decleva, and F. Martín, Proc. Natl. Acad. Sci. U. S. A. **108**, 7302 (2011).
[9] E. Shigemasa, J. Adachi, M. Oura, and A. Yagishita, Phys. Rev. Lett. **74**, 359 (1995).
[10] R. K. Kushawaha, M. Patanen, R. Guillemin, L. Journel, C. Miron, M. Simon, M. N. Piancastelli, C. Skates, and P. Decleva, Proc. Natl. Acad. Sci. U. S. A. **110**, 15201 (2013).
[11] M. Kunitski, N. Eicke, P. Huber, J. Köhler, S. Zeller, J. Voigtsberger, N. Schlott, K. Henrichs, H. Sann, F. Trinter, L. Ph.H. Schmidt, A. Kalinin, M. S. Schöffler, T. Jahnke, M. Lein, and R. Dörner, Nat. Commun. **10**, 1 (2019).
[12] J. Cooper and R. N. Zare, J. Chem. Phys. **48**, 942 (1968).
[13] A. Sanov, Annu. Rev. Phys. Chem. **65**, 341 (2014).
[14] H. D. Cohen and U. Fano, Phys. Rev. **150**, 30 (1966).
[15] O. Fojón, J. Fernández, A. Palacios, R. Rivarola, and F. Martin, J. Phys. B **37**, 3035 (2004).
[16] B. Zimmermann, D. Rolles, B. Langer, R. Hentges, M. Braune, S. Cvejanovic, O. Geßner, F. Heiser, S. Korica, and T. Lischke, Nat. Phys. **4**, 649 (2008).
[17] D. Akoury, K. Kreidi, T. Jahnke, T. Weber, A. Staudte, M. Schoffler, N. Neumann, J. Titze, L. P. H. Schmidt, A. Czasch, O. Jagutzki, R. A. C. Fraga, R. E. Grisenti, R. D. Muino, N. A. Cherepkov, S. K. Semenov, P. Ranitovic, C. L. Cocke, T. Osipov, H. Adaniya, J. C. Thompson, M. H. Prior, A. Belkacem, A. L. Landers, H. Schmidt-Bocking, and R. Dorner, Science **318**, 949 (2007).
[18] D. Dill, J. Chem. Phys. **65**, 1130 (1976).
[19] M. J. S. Dewar, Proc. Camb. Philos. Soc. **45**, 638 (1949).
[20] R. Mabbs, E. Surber, L. Velarde, and A. Sanov, J. Chem. Phys. **120**, 5148 (2004).
[21] R. Mabbs, K. Pichugin, and A. Sanov, J. Chem. Phys. **123**, 054329 (2005).
[22] A. Sanov and R. Mabbs, Int. Rev. Phys. Chem. **27**, 53 (2008).
[23] L. De Broglie, Nature **112**, 540 (1923).
[24] G. W. Spitznagel, T. Clark, J. Chandrasekhar, and P. V. R. Schleyer, J. Comput. Chem. **3**, 363 (1982).
[25] C. M. Oana and A. I. Krylov, J. Chem. Phys. **131**, 124114 (2009).
[26] Y. Liu and C. G. Ning, J. Chem. Phys. **143**, 144310 (2015).
[27] H. T. Liu, C. G. Ning, D. L. Huang, and L. S. Wang, Angew. Chem., Int. Ed. **53**, 2464 (2014).
[28] R. L. Tang, X. X. Fu, and C. G. Ning, J. Chem. Phys. **149**, 134304 (2018).
[29] M. L. Weichman and D. M. Neumark, Annu. Rev. Phys. Chem. **69**, 101 (2018).
[30] S. J. Cavanagh, S. T. Gibson, M. N. Gale, C. J. Dedman, E. H. Roberts, and B. R. Lewis, Phys. Rev. A **76**, 052708 (2007).
[31] S. H. Vosko, L. Wilk, and M. Nusair, Can. J. Phys. **58**, 1200 (1980).
[32] C. Lee, W. Yang, and R. G. Parr, Phys. Rev. B **37**, 785 (1988).
[33] A. D. Becke, J. Chem. Phys. **98**, 5648 (1993).
[34] P. Stephens, F. Devlin, C. Chabalowski, and M. J. Frisch, J. Phys. Chem. **98**, 11623 (1994).
[35] ADF2018, SCM, Theoretical Chemistry, Vrije Universiteit, Amsterdam, The Netherlands, http://www.scm.com.
[36] M. J. Frisch, G. W. Trucks, H. B. Schlegel, G. E. Scuseria, M. A. Robb, J. R. Cheeseman, G. Scalmani, V. Barone, B. Mennucci, G. A. Petersson, H. Nakatsuji, M. Caricato, X. Li, H. P. Hratchian, A. F. Izmaylov, J. Bloino, G. Zheng, J. L. Sonnenberg, M. Hada, M. Ehara, K. Toyota, R. Fukuda, J. Hasegawa, M. Ishida, T. Nakajima, Y. Honda, O. Kitao, H. Nakai, T. Vreven, J. A. Montgomery, Jr., J. E. Peralta, F. Ogliaro, M. Bearpark, J. J. Heyd, E. Brothers, K. N. Kudin, V. N. Staroverov, R. Kobayashi, J. Normand, K. Raghavachari, A. Rendell, J. C. Burant, S. S. Iyengar, J. Tomasi, M. Cossi, N. Rega, J. M. Millam, M. Klene, J. E. Knox, J. B. Cross, V. Bakken, C. Adamo, J. Jaramillo, R. Gomperts, R. E. Stratmann, O. Yazyev, A. J. Austin, R. Cammi, C. Pomelli, J. W. Ochterski, R. L. Martin, K. Morokuma, V. G. Zakrzewski, G. A. Voth, P. Salvador, J. J. Dannenberg, S. Dapprich, A. D. Daniels, Ö. Farkas, J. B. Foresman, J. V. Ortiz, J. Cioslowski, and D. J. Fox, GAUSSIAN 09, Revision D.01, Gaussian, Inc., Wallingford, CT, 2009.
[37] T. Koopmans, Physica **1**, 104 (1934).
[38] I. Dabo, A. Ferretti, N. Poilvert, Y. L. Li, N. Marzari, and M. Cococcioni, Phys. Rev. B **82**, 115121 (2010).
[39] H. Sakai, C. P. Safvan, J. J. Larsen, K. M. Hilligsoe, K. Hald, and H. Stapelfeldt, J. Chem. Phys. **110**, 10235 (1999).
[40] J. Itatani, J. Levesque, D. Zeidler, H. Niikura, H. Pepin, J. C. Kieffer, P. B. Corkum, and D. M. Villeneuve, Nature **432**, 867 (2004).
[41] L. Holmegaard, J. L. Hansen, L. Kalhøj, S. L. Kragh, H. Stapelfeldt, F. Filsinger, J. Küpper, G. Meijer, D. Dimitrovski, and M. Abu-Samha, Nat. Phys. **6**, 428 (2010).
[42] R. Mabbs, F. Mbaiwa, J. Wei, M. Van Duzor, S. T. Gibson, S. J. Cavanagh, and B. R. Lewis, Phys. Rev. A **82**, 011401(R) (2010).
[43] M. S. Schöffler, K. Kreidi, D. Akoury, T. Jahnke, A. Staudte, N. Neumann, J. Titze, L. Ph. H. Schmidt, A. Czasch, O. Jagutzki, R. A. Costa Fraga, R. E. Grisenti, M. Smolarski, P. Ranitovic, C. L. Cocke, T. Osipov, H. Adaniya, S. Lee, J. C. Thompson, M. H. Prior, A. Belkacem, Th. Weber, A. Landers, H. Schmidt-Böcking, and R. Dörner, Phys. Rev. A **78**, 013414 (2008).
[44] A. K. Mills, S. Zhdanovich, E. Rampi, R. Comin, G. Levy, A. Damascelli, and D. J. Jones, *CLEO: 2014*, OSA Technical Digest (Online) (Optical Society of America, 2014), paper FM4B.6.